Contributions to Mineralogy and Petrology (2024) 179:38
https://doi.org/10.1007/s00410-024-02128-x

ORIGINAL PAPER

Towards an integrated texture toolkit, 1: unveiling the complex relationship between crystal shape and fabric in EBSD data

Ryan M. Currier[1] · **Tushar Mittal**[2] · **Paulo J. Hidalgo**[3]

Received: 1 December 2023 / Accepted: 24 March 2024

Abstract

Rock textures observed via thin section are skewed from their true 3D nature. This is due to various cut effects—artifacts introduced due to the lower dimensional nature of the thin section relative to the rock. These cut effects can be corrected, and several methods have been developed to invert crystal shape and crystal size, but with each process performed separately and sequentially. With the ongoing adoption of electron backscatter diffraction (EBSD) by petrologists, an additional data stream has now become available: the 3D orientation of 2D grain sections. For EBSD analysis, no stereological corrections are typically applied for interpreting the data. This study tests whether this orientational information is skewed due to a fabric cut effect. We test this by numerically generating synthetic crystal datasets representative of several crystal shapes and population sizes. We find that EBSD orientational data has a fabric cut effect since crystals oriented with long axes perpendicular to the thin section are more likely to be sampled compared to those with long axes oriented parallel to it. This effect must be accounted for to interpret the true 3D fabric accurately. Towards this end, we develop two new tools for working with EBSD-derived fabric: (1) a simple first-order test for determining if a measured fabric exceeds that of the fabric cut effect, and (2) a method of inverting cut fabrics that provides robust error estimations. We demonstrate the applicability and accuracy of these methods using a range of synthetic examples and a natural sample. With these newly developed tools, there is clear potential for a new textural toolkit framework, to further our ability to correct for the various cut effects while also providing accurate uncertainty estimates.

Keywords Rock fabric · Rock texture · Texture analysis · Stereology · EBSD

Introduction

Rock texture encapsulates the spatial and geometric characteristics of elements within the rock. Particle shape, size, and orientation are all examples of textural features. The textural information is, in turn, a critical observational input for characterizing the physical properties of geomaterials and understanding the processes associated with forming the constituent minerals. For instance, rock textural features encode many physical properties of the rock, such as seismic wave speed (Frothingham et al. 2023), thermal expansivity (Gibert et al. 2003), fluid permeability (Urumovic and Urumovic 2014), and mechanical strength (Prikryl 2006). Additionally, in igneous rocks, the mineral grain shape and size are functions of the cooling rate (Mangler et al. 2022; Marsh, 1998), while orientations can encode the kinematic history (e.g. magmatic sense of shear: Vukmanovic et al. 2018; compaction: Jenkins et al. 2022; grain clustering mechanisms: Holness et al. 2023). Similar applications can be extended into metamorphic systems with rock fabric encoding the deformation history and behavior (e.g., Fossen and Cavalcante 2017), fluid reactivity with primary minerals (Andreani et al. 2009), as well as biosphere/geosphere interaction (Hemkemeyer et al. 2018).

Historically, most textural analyses have been performed in thin sections or on polished surfaces, by measuring the

Communicated by Dante Canil.

✉ Ryan M. Currier
rcurrier@westga.edu

[1] Department of Natural Sciences, University of West Georgia, 1601 Maple St, Carrollton, GA 30118, USA

[2] Department of Geosciences, Pennsylvania State University, 116 Deike Building, University Park, PA 16802, USA

[3] Department of Geosciences, Georgia State University, 38 Peachtree Center Ave. SE 7th Floor Suite 730, Atlanta, GA 30303, USA

2D outlines of the intersection between a crystal and the thin section. This methodology requires little instrumentation—a petrographic microscope and illustration software—so the entry cost is minimal. Over the past few decades, there have been significant improvements - both on the instrumental side (e.g., digital microscopy, EBSD: electron backscatter diffraction, QEMSCAN: quantitative evaluation of materials by scanning electron microscopy), as well as data analysis methods (e.g., image segmentation, shape and spatial analysis), in characterizing the rock microtexture and rapid processing of large datasets. However, there is still inherently a fundamental challenge with all these methods of textural analysis on a thin section: converting 2D in-plane measurements to 3D estimates using stereological correction techniques. To overcome this challenge, 3D imaging techniques like X-ray tomography have been developed for textural analysis (Jerram and Higgins 2007; Jerram et al. 2010; Lanzafame et al. 2017; Polacci et al. 2018). However, these techniques are inherently data intensive (both in terms of collection and processing) and expensive. Hence, they are not eminently scalable or readily accessible to most of the geoscience community. Thus, 2D thin section analysis remains the dominant and most accessible form of textural analysis.

The challenges associated with accurate stereological (2D to 3D) analysis have been known for decades (Higgins 1994; Howard and Reed 1998; Saltikov 1967; Underwood 1969). Several stereological 2D to 3D correction tools have been developed based on these, especially in the igneous petrology community (e.g., CSDCorrections: Higgins 2000; CSDslice: Morgan and Jerram 2006; ShapeCalc: Mangler et al. 2022). The 2D crystal size is by far the most analyzed parameter, corresponding to the areal intersection of a 3D crystal with the cutting plane of the section. The 3D shape of crystals can be derived from 2D measurements by adopting different stereological approaches. However, these existing tools for stereological corrections are based on several simplifying, but hidden assumptions that may need to be revised for each dataset. For instance, analysis methods frequently assume that crystal shape is constant across all crystal sizes, whereas this can potentially vary across the population (Mock and Jerram 2005), or as a function of crystal size (Dunbar et al. 1995; Mangler et al. 2022). Analogously, the tools typically do not provide the full uncertainty covariance matrix between shape, size, and orientation. In addition, these prepacked tools are typically not fully open source, and without access to the underlying code for analysis and synthetic crystal cut generation, significant barriers are present for users to make modifications as needed for their geologic context and datasets.

There is thus a need for an open source, well-documented, validated, and extendable textural analysis toolkit for thin section analysis with two key aims: (I) accurate stereological textural corrections, with associated uncertainties, for shape, size, and orientations, and (II) flexibility to incorporate multiple types of thin section datasets jointly (i.e. electron beam methodologies as well as different optical methodologies such as reflected light with different Illumination angles, transmitted light, and cross-polarized with multiple orientations). The need for this textural toolkit is, in particular, becoming increasingly relevant since two mature methodologies are capable of automated grain analysis within the Scanning Electron Microscope (SEM. QEMSCAN utilizes chemical analyses to identify phases, and can produce grain maps based on these chemical differences. Another technique, EBSD, utilizes electron diffraction patterns by the crystal lattice to determine phase and crystal lattice orientation to segment grains (for review, see: Britton et al. 2016). One of the benefits of EBSD analysis is that it can be used for automated grain segmentation based on the principle of localized orientation clustering within a single crystal (Cone et al. 2020). Thus, EBSD datasets address some of the key practical challenges with classical thin section analysis: (a) collecting statistically significant datasets via manual crystal tracing is time consuming, and (b) these datasets are prone to error because crystal boundaries are often subjective and thus susceptible to person to person variance.

EBSD, compared to QEMSCAN, CT-scans, and traditional optical methods, provides an additional data stream, namely that of 3D crystal lattice orientations of 2D crystal intersections, which yields a 2.5D map of rock texture. In this study, we focus on EBSD analyses, because the orientation information represents an additional, hitherto unexplored, data stream that can be leveraged to more fully characterize rock texture. In particular, this paper focuses on the following question: *What are the (if any) stereological biases that can be present when analyzing the crystal orientation datasets from EBSD?* An increasing number of studies are using EBSD for rock textural analysis (Bernard et al. 2023; Bertolett et al. 2019; Casale et al. 2023; Cross et al. 2017; Holness et al. 2023; Koyama et al. 2023; Rehman et al. 2023; Wieser et al. 2019). However, in contrast to 2D thin section size-shape analysis, the need for stereological corrections with EBSD orientation datasets hasn't been thoroughly scrutinized. Our study addresses this critical knowledge gap and illustrates that the EBSD data does display a "fabric" cut effect that must be corrected for, especially in samples with weak fabric (e.g., magmatic systems). This illustrates one of the necessary components for a next-generation textural toolkit.

We begin with a brief review of stereological artifacts, followed by the methodologies employed in EBSD and our modeling. Following this, we present results from

synthetically developed rock textures and develop an inversion algorithm to correct the fabric-cut effect. Finally, we apply our methodological approach to a natural sample and discuss the key challenges to further developing the textural toolkit.

Background

A 2D slice of a 3D object represents a loss of dimension, and, consequently, loss of information about the 3D structure of the object. The observable data in a 2D slice deviates from the true 3D quantity (or, likewise, 1D slices of 2D shapes). This is known as a *cut effect*. The goal of stereology is to correct these cut effects, allowing for a more robust interpretation of the 3D characteristics of a sample from a 2D cross-section view. Several cut effects become embedded in the 2D information offered by the cross-section. While these are typically lumped into a catch-all term, *the* cut effect, we decompose this general term and explicitly detail each type. Although slightly pedantic, the following text clearly describes the different types of cut effects to highlight how the fabric-cut effect is distinct from previous work.

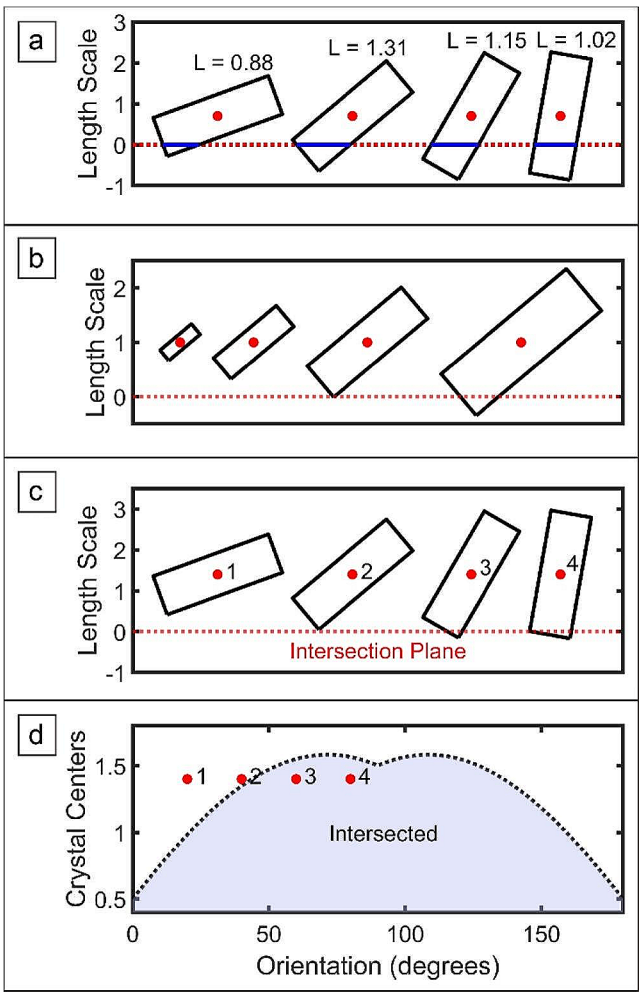

Fig. 1 Simplified, 2D examples of cut-effects. (a) Slices of cut shapes are lower dimensional features (here: 1D line segments), which are skewed from the true higher dimensional shape. (b) The cut disproportionately samples crystals of different shapes (not shown) or sizes (shown), despite other variables being controlled for. (c) The Fabric Cut-Effect is the disproportionate sampling of crystals on the basis of orientation, indicating that the apparent fabric of a slice is skewed from the true higher-dimensional fabric. (d) The sampling space for a 2D shape with long axis, L: 3, and short axis, S: 1 dependent on shape-cut distance (y-axis) and long axis orientation relative to the cut (x-axis). Numbered points correspond to the oriented shapes in C

Size-cut effect

The apparent size of a cut particle (i.e. crystal, grain, or otherwise) is dependent on the orientation of the particle, as well as its extra-dimensional location relative to the cut. This results in a range of potential apparent sizes for a particle. For a random underlying distribution of particle orientations and centers, the size-cut effect results in a distribution of apparent sizes, even if the underlying size is the same for all particles (Fig. 1a). Because the apparent size of a particle offered in a slice can never be larger than the true size of the particle, the size cut effects often makes particles appear smaller than reality.

Size-distribution-cut effect

For a unit area or a unit volume, a 1D and 2D cut section, respectively, is more likely to intersect a large particle than a small particle (Fig. 1b). For a distribution of particle sizes, a slice thus disproportionately samples larger particles. This leads to a bias in the measurement of particle size distribution in a 2D thin section compared to the 3D size distribution with apparent too many small particles in the measured 2D cut (analogous to 1D). This cuteffect has also been referred to as the "Intersection-Probability Effect"(Higgins 1994).

Shape-cut effect

Depending on how a particle is sliced, the resulting lower dimension shape is not representative of the true shape of the particle for a large proportion of potential slices. Thus, the measurements of particle shape descriptors such as aspect ratio, ellipticity, particle area, Feret diameter, etc., would also be biased compared to the true 3D distributions. The potential shape-cut effect becomes increasingly significant as the particle shape deviates from sphericity.

Fabric-cut effect

For a collection of distributed particle orientation, particles are more likely to be intersected when their long axis is perpendicular to the thin section, and less likely when the long axis is in plane with the thin section (Fig. 1c). An intersection phase diagram (Fig. 1d) can be mapped by varying the distance between particle centers and the cut, then rotating the particles and testing for intersection. In this example, the particles are rectangles (Long: 3, Short: 1), and it can be observed that as the orientation of the rectangle's long axis approaches perpendicular to the intersection line, they are sampled by the cut from greater distances. For a uniform distribution of particle orientations and particle centers, the result is an apparent fabric with long axes oriented perpendicular to the cut.

These cut effects do not exist in isolation from each other. Instead, the *overall* cut effect is a function of each cut effect, coupled with the others. If we care about the fabric of the sample as a microstructural quantity, then all cut effects must be self-consistently accounted for. Even if we use data collected via EBSD, which provides crystallographic orientations directly, and hence nominally the micro-textural fabric, *the EBSD results still need to account for the fabric cut effect.*

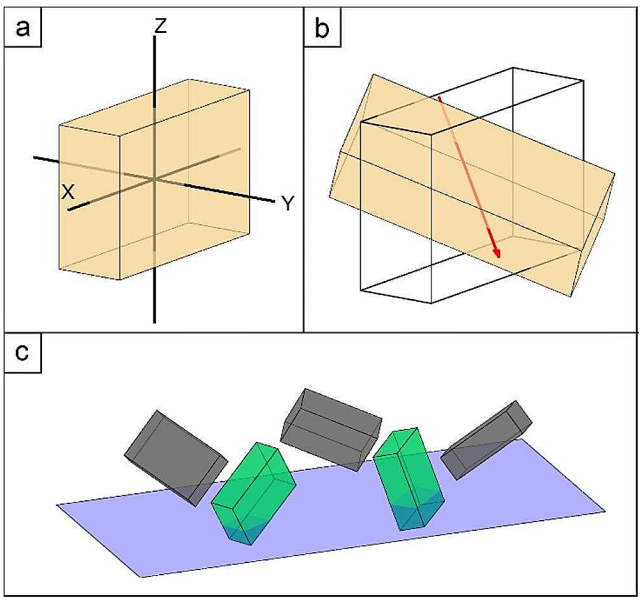

Fig. 2 Synthetic ODF Algorithm. (a) 3D shapes are generated with crystallographic axes tied to coordinate axes. The crystal shape shown is A:3 B:2 C:1. (b) After choosing a rotation, the vertices of the 3D shape are rotated, shown here using a unit quaternion (the red vector is the rotation axis defined by the vector portion of the quaternion). (c) Rotated shapes are immersed into a volume with cut plane shown in purple. The orientations are collected from the shapes which intersect the cut plane (Green), and discarded when the shapes do not intersect the cut plane (Black)

While the shape-, size-, and size-distribution-cut effects have been analyzed in previous studies, a careful analysis of the fabric-cut effect and methods to correct it currently needs improvement. The fabric-cut effect forms the basis of this study. An investigation of the fabric-cut effect is presented here, followed by tools to interpret and process EBSD fabrics. The first tool is a simple method for characterizing fabrics, testing whether the cut fabric is consistent with either uniform or non-uniform orientations. The second is a method for inverting the cut effect to construct a representation of the underlying 3D fabric using a synthetic forward modeling approach.

The number of measured crystal orientation is an additional potentially influential effect on results. There is ever only a finite number of measurements of crystals within a single sample, and depending on whether the data is acquired manually or in an automated fashion, the sample size can vary markedly. Thus, the effects of crystal numbers include additional uncertainties in inversion methods when correcting for all the stereological cut effects.

Methods

Following existing work in this field, we follow the general outline for modelling the cut effect of grain shape (Higgins 1994; Morgan and Jerram 2006; Mangler et al. 2022). At the heart of these 3D shape estimators is a catalog of 2D intersection data from known 3D shapes that have been randomly rotated and randomly distributed in a volume, such that all particles are free to "miss" the intersection plane, and only 2D data from intersections are collected (see Fig. 2 for the different steps, and Online Resource for a thorough description). The ODF relates the areal proportion (A) of an orientation (r) over the orientation space.

$$ODF\,(r) = \frac{1}{A}\frac{dA\,(r)}{dr} \tag{1}$$

Following standard convention in the literature, we express the values over the ODF in terms of multiples of a uniform distribution (MUD). Thus, a genuinely uniform distribution will have a value of MUD = 1 over orientation space. One can conceptualize the ODF as similar to a probability distribution function wrapped over orientation space. In this study, the ODFs are constructed using one orientation measurement per grain rather than orientations per unit area of the 2D crystals (which is analogous to sampling per unit area of the thin section). This choice removes the effect of disperse crystal sizes in the sample, where larger grains would disproportionately impact the resultant fabric analysis due

to more sampled orientation points for their larger cross-sectional area. We utilize the J-index to quantify the strength of the fabric (Mainprice et al. 2015). J-index is defined as:

$$J = \int ODF\,(r)^2 dr \tag{2}$$

J-Index ranges from 1 (uniformly distributed) to infinity (single crystal fabric).

Results

Fabric -cut effect on a uniform ODF

A crystallographic system needs to be selected to generate synthetic pole figures to visualize the distribution of orientations. To begin, we choose the simple orthorhombic crystal system (α = β = γ = 90°). The resulting pole figures from the Uniform ODF are shown in Fig. 3a, with MUD ≈ 1 across the stereoplot for all axes.

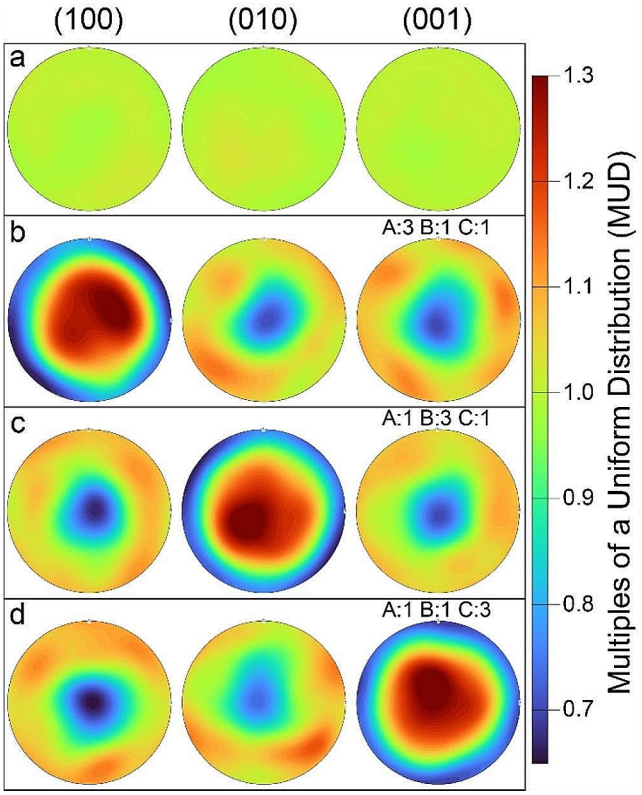

Fig. 3 ODFs of $n = 3000$ prolate crystals (L:3, I: S:1, with L = long axis, I = intermediate axis, and S = short axis) before cutting (a), and after cutting (b-d). Colorbar is in units of Multiples of a Uniform Distribution (MUD) and is equal for all ODFs. (a) The true fabric of the system (uncut fabric) displays no discernible structure across each crystallographic axis, with MUD ~ 1. (b) Cut fabric, crystal shape is A: 3, B: 1, C: 1 (i.e., A = L, and B = C = I = S). (c) Cut fabric, crystal shape is A: 1, B: 3, C: 1 (i.e., B = L, and A = C = I = S). (d) Cut fabric, crystal shape is A: 1, B: 1, C: 3 (i.e., C = L, and A = B = I = S). Note: all cut fabrics display a vertical pole along the corresponding crystallographically controlled long-axis of the crystal, and girdles for the other crystallographic axes

Cutting the crystals that comprise the Uniform ODF results in the development of non-uniform fabric, depending upon the crystal shape (Fig. 3). Considering the cut ODF for crystal shape A: 3, B: 1, C: 1, the apparent fabric is a vertically aligned pole along the A-axis (and the pole to the face (100)), and horizontal girdles for the B- and C-axes (and the respective poles to faces (010) and (001)). Because the crystal morphology and orientations are controlled as input, we can directly connect the crystal shape and the resulting cut fabric. The pole perpendicular to the intersection plane coincides with the crystal long axis (A = 3), and girdles for the short axes (B = C = 1). From the simple 2D analogy illustrated in Fig. 1d, it is clear that the vertical pole for the A-axis, (100), is due to the higher probability of intersecting crystals when the long axis is perpendicular to the intersection plane, skewing the distribution of observed orientations. A simple deduction is that in uniformly distributed orientations, the cut effect results in a pole along the long axis of the crystal (Fig. 3).

While the above treatment demonstrates that the cut effect produces artifacts in the ODF for anisotropic crystal shapes, the results can be made more realistic by taking into consideration the interaxial angles of the commonly analyzed crystal system, plagioclase (triclinic: e.g., Anorthite, α = 93.166°, β = 115.85°, γ = 91.216°). Supplementary information provided in the Online Resource thoroughly describes how synthetic plagioclase crystals are generated. Accounting for the interaxial angles slightly modifies the resultant pole figures (Fig. 4). In this case, the crystal shape is A: 3, B: 1, C: 1. The fabric-cut effect imposes a vertical pole along the A-axis, (100), a horizontal girdle for the B-axis, (010), and a weaker, inclined girdle for the C-axis, (001). The inclination of the C-axis girdle is due to the larger interaxial angle between the A- and C-axes (β = 115.85°). *We note that this fabric-cut effect would also persist for non-uniform ODF scenarios except that the pole peak and girdle pattern above would be combined with the underlying non-uniform orientation distribution.*

Quantifying the fabric-cut effect

The fabric-cut effect increases the fabric strength for input uniformly distributed crystal orientations. In the following, we propose that the J-Index of a sample can be used to measure whether the underlying fabric is uniform. Several variables need to be constrained: (1) the effect of crystal numbers (2) the effect of crystal symmetry, and (3) the effect of crystal shape.

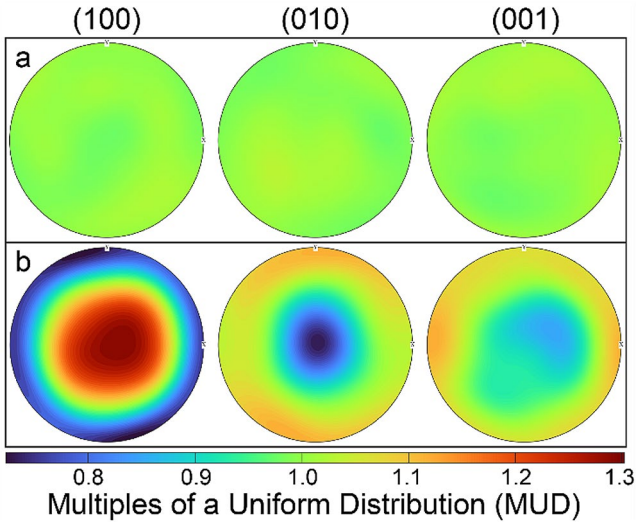

Fig. 4 ODFs of $n = 3000$ prolate, triclinic crystals, prior to cutting (a), and after cutting (b). Colorbar is in units of Multiples of a Uniform Distribution (MUD) and is equal for all ODFs. (a) The true fabric of the system (uncut fabric) displays no discernible structure across each crystallographic axis, with MUD ~ 1. (b) Cut fabric, crystal shape is A: 3, B: 1, C: 1

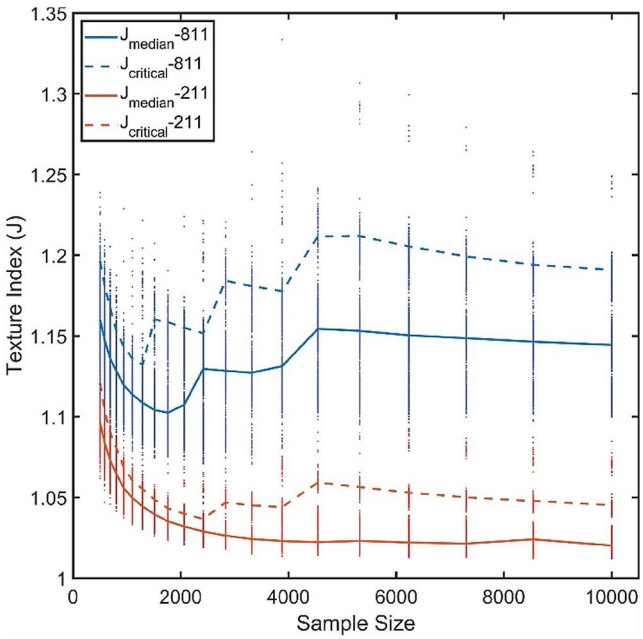

Fig. 5 Effect of Sample Size on Texture Strength of Cut Fabrics. Data in blue corresponds to crystal shape A: 8, B: 1, C: 1, while red A: 2, B: 1, C: 1. For each sample size, 1000 runs were performed (datapoints). As observed by the median and critical texture index values, the J-Index generally decreases with increasing crystal count, and asymptotically converges towards the infinite sample size case. Variations in this trend (i.e. the upwards "stair-stepping" in texture index) is an artifact associated with the kernel optimization algorithm, where bandwidth increases and kernel halfwidth decreases with increasing sample size, resulting in slight increases in texture strength

Effect of crystal numbers

Sample size (number of crystals) affects the J-Index because we are fitting a continuous ODF to discrete orientation measurements. Fewer measurements can result in poorer fits, resulting in more pronounced fabric. Taken to its extreme, a single crystal orientation will produce a J-Index of infinity, and on the other extreme, approaching an infinite number of crystal orientation measurements will converge on the true texture strength. We test this effect of sample size on texture strength by keeping the crystal shape constant and the orientation distribution uniform, while varying sample size and repeating the process 1000 times for each combination of shape and sample size (Fig. 5).

The median texture index for each combination of shape and sample size (J_{median}) and the 95% threshold ($J_{critical}$) are shown. The impact of the fabric cut effect is most prominent for small sample sizes, while with increasing sample size, asymptotically converges towards a constant as a function of crystal shape. Beyond ~ 2000 crystal orientations sampled, the effect of increasing sample size for a uniform underlying ODF is minimal. Note, that with increasing sample size, there is an additional effect from variations in the optimized kernel halfwidth. As sample size increases, kernel halfwidth tends to decrease, which can result in an increase in measured J-index. These are observed in Fig. 5 as "stair-steps" towards increasing sample size. However, after each of these jumps, the overall asymptotically decreasing J-index trend with increasing sample size resumes. The asymptote is the J-index value of the infinite sample size ODF for each crystal shape.

We have chosen a large enough sample size to be approximately within the asymptotic tail region for J-index values but small enough to be applicable for many geologically relevant investigations. Certainly, coarse-grained sample sizes are fundamentally limited by the size of the thin-section. The general approach outlined here is valid for small sample sizes, but confidence intervals would edge towards the minimum sample size limit (i.e., 1) in Fig. 5. As the sample size decreases, the J-index increases rapidly, with the J-index for all crystal shapes converging at infinity for $n = 1$. In the small sample size region, the variance of J-index values corresponding to different crystal shapes begin to overlap and, towards the limit, become indistinct.

Effect of crystal symmetry

The effect of the fabric-cut effect on crystal symmetry is tested by comparing orthorhombic crystal symmetry to triclinic crystal symmetry (i.e. plagioclase, as above), by holding both crystal axial ratios and sample size constant ($n = 3000$ crystals), and repeating the process 1000 times.

Results are shown in the accompanying Online Resource (Supplementary Fig. 2) as a comparison plot by crystal symmetry. J_{median} and $J_{critical}$ fall close to a line of slope = 1 for very different input crystal shapes, indicating that the crystal symmetry does not play a first-order role in the fabric-cut effect. Thus, our inversion methods (described later) should apply broadly.

Effect of crystal shape

We repeat the same synthetic sectioning analysis as above to test the effect of crystal shape on the resulting cut fabric strength. Crystal shapes are iterated over a wide range of crystal shape space (A/C = 0.1:10; B/C = 0.1:10), and the sample size is held constant at $n = 3000$. The median (J_{median}) and 95% threshold ($J_{critical}$) values are color coded in Fig. 6a and b. In general, as crystal shape becomes more prismatic, the fabric-cut effect becomes more pronounced. The results are roughly the same, independent of which crystal axis is the long axis. To illustrate the physical relevance of the chosen crystal morphologies, we overplot the morphology of relevant igneous phases (Fig. 6d).

If the crystal shape can be relatively well-constrained (e.g., using ShapeCalc), then the J-index of the ODF collected from 2D analysis indicate whether the true, uncut fabric is uniformly distributed. For most crystal shapes, we find that if the J-index of the 2D analysis is greater than ~ 1.2 then the uncut fabric is not uniformly distributed (i.e., there exists a directionally oriented fabric). However, for weaker fabrics, a more precise approach is warranted. To facilitate this process, we fit a 3rd-order polynomial to the results of the fabric-cut effect on crystal shape. The overall fits of these polynomial surfaces are quite good, as indicated by the minimal difference between color-coded datapoints and background polynomial estimation (Fig. 6a-c), as well as the large R^2 values (J_{median}, Fig. 6a: $R^2 = 0.944$; $J_{critical}$, Fig. 6b: $R^2 = 0.946$; $J_{critical}$, Fig. 6c: $R^2 = 0.991$;). To utilize this polynomial, coefficients are presented in Table 1, and are input into the following equation:

$$J_i = C + X + Y + X^2 + XY + Y^2 + X^3 + X^2Y + XY^2 + Y^3 \quad (3)$$

Where values of X and Y depend on whether crystallographic space is considered (X = ln(A/C), Y = ln(B/C)), or Zingg space is considered (X = S/I, Y = I/L), and Ji corresponds to the chosen quantity of J to be quantified (i.e., the chosen column in Table 1). The results are interpreted using:

$J <= J_{critical:}$: Uncut ODF is uniform

$J > J_{critical:}$ Uncut ODF is not uniform

It is important to note that other cut effects (e.g., size distribution), or deviations from our assumptions (e.g. uniform crystal shape) may influence the results presented in this section. For example, if different crystal size populations possess different fabric characteristics, the size-distribution-cut effect could contribute to the measured ODF.

Inverting the fabric cut effect

For a single crystal, and considering only the fabric-cut effect, the probability of the crystal intersecting the cut plane is a function of the crystal shape (sh) and crystal orientation (ori). *The fabric-cut effect is simply this relationship integrated over all possible orientations*. The cut probability, p_{cut}(sh, ori) is taken as the ratio of the vertical profile (i.e., the length between the maximum and minimum vertical points) of an oriented crystal, h_{ori}, to the maximum distance between antipodal vertices of the crystal, h_{max}:

$$p_{cut} = \frac{h_{ori}}{h_{max}} \quad (4)$$

Where h_{max} is the maximum vertical profile for a given crystal shape, and the linear distance from the cut plane such that all possible crystal orientations can miss the cut plane. These relationships are illustrated in the Online Resource (Supplemental Fig. 3). Note that while the true probability of a crystal intersecting a cut plane will also account for crystal size, this is a consequence of the size-distribution-cut effect. However, assuming there is no variation in the fabric across crystal sizes, absolute size does not impact this probability.

The intersection probability for each crystal orientation, measured from a cut fabric, is modeled using an input crystal shape. The number of crystals of each orientation in the uncut fabric, N_{uncut} (per each observed crystal of a given orientation) is the inverse of the probability of cutting each orientation from the cut fabric.

$$N_{uncut} = \frac{1}{p_{cut}} \quad (5)$$

Because crystal numbers are strictly whole numbers, the value of N_{uncut} is multiplied by 100 and rounded to generate two significant digits of precision. We choose an uncertainty threshold of $\sigma = 2.5°$ and apply a three-dimensional Gaussian to blur the inverted orientation slightly. This avoids large crystal counts of the same orientation. All ODFs generated from these inversions are produced using kernel halfwidths all greater than the chosen 2.5° randomization.

What we have detailed above assumes a *perfect inversion* scenario. In a natural system, packing effects in a 3D volume

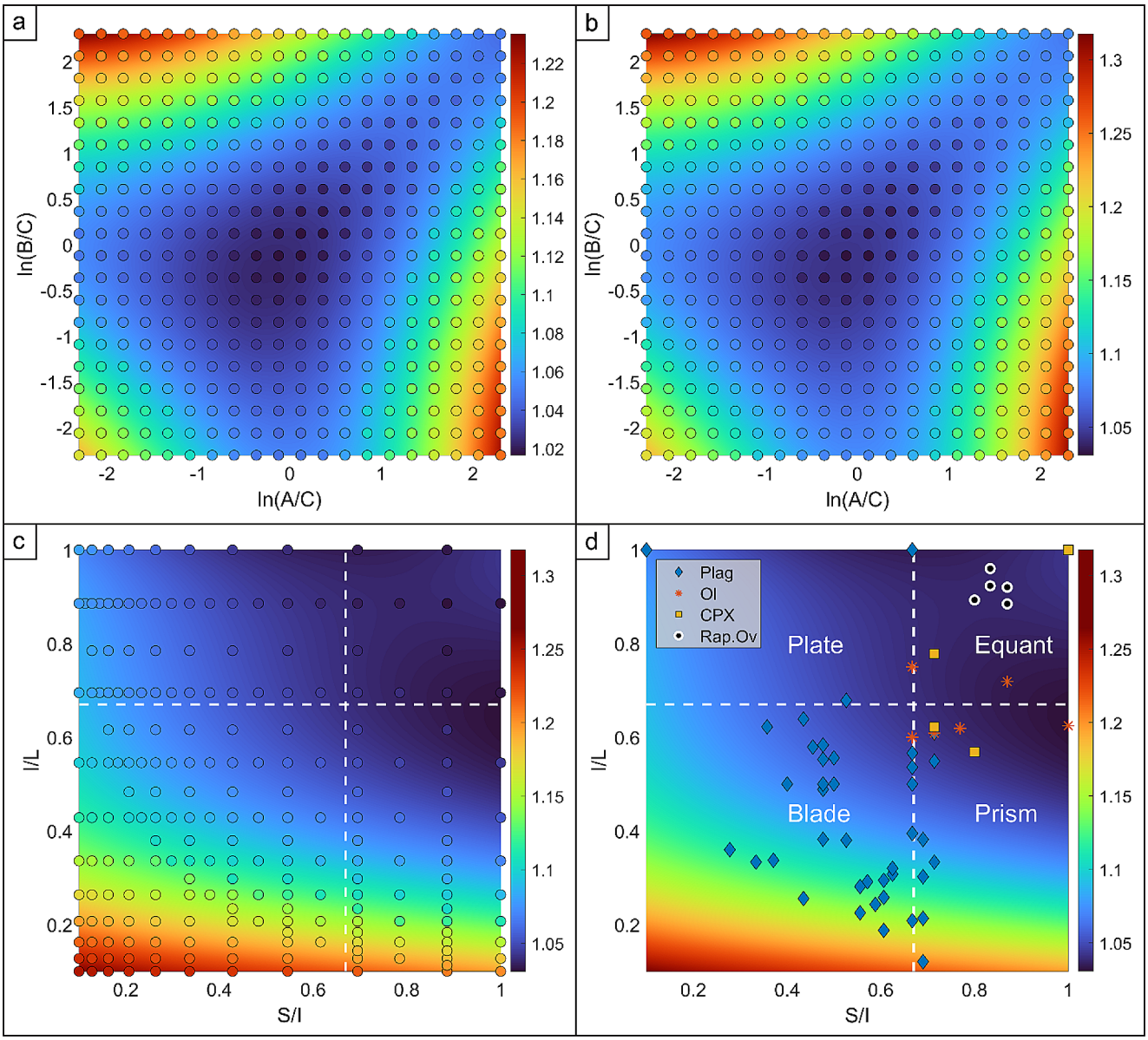

Fig. 6 Effect of crystal shape on texture strength. surfaces fit to results from 1000 runs at each interrogation morphology, with 3000 crystals for each run. coefficients for the third-order polynomials that describe these surfaces are provided in Table 1. datapoints in panels a-c represent input crystal morphologies, and have been color-coded to the same range as the fit surface (background color). (a) color map of the median texture index value (J_{median}). (b) color map of the 95th percentile texture index ($J_{critical}$). C) the results displayed in panel b, but translated to Zingg diagram space. S/I = Short/Intermediate. I/L = Intermediate/Long. Dashed lines represent divisions in shapes: quadrant I: Equant, II: Plate, III: Blade, IV: Prism. d) shape estimates for plagioclase, olivine, clinopyroxene, and rapakivied feldspar ovoids (Bain et al. 2019; Brugger and Hammer 2010; Currier et al. 2019; Higgins 2002; Magee et al. 2010; Muncill and Lasaga 1988; Ngonge et al. 2013; Phillips et al. 2013; Salisbury et al. 2008; Vinet and Higgins 2011)

will affect these probabilities. So, we also allow for some stochastic variation in the inversion. This *imperfect inversion* method is accomplished by generating a long vector of random numbers sampled from a uniform probability distribution for each associated crystal, and then determining the first element within this array where the random number value is less than each crystal's calculated p_{cut} value. The count of random numbers necessary to satisfy this condition is taken as N_{uncut} for the crystal in question. The process follows as in the *perfect inversion* scenario, where orientations are randomized using a three-dimensional Gaussian with $\sigma = 2.5°$, and the ODF is constructed. This process is repeated ($n = 1000$), with each repetition an *imperfect inversion* result. Overall, the *imperfect inversion* process is akin to bootstrapping (a common statistical analysis method), to estimate the inherent variation associated with the inversion

Table 1 Coefficients and associated leading terms of the third-order polynomial surface fit to J_{median} and $J_{critical}$ results across crystal morphology space, for relatively large sample sets. For crystallographic space: X = ln(A/C) and Y = ln(B/C). For Zingg space: X = S/I, Y = I/L

Term	J_{median} (ABC)	$J_{critical}$ (ABC)	$J_{critical}$ (Zingg)
C	1.025	1.045	1.359
x	0.00356	0.004331	-0.09895
y	0.00578	0.00669	-0.9557
x^2	0.0132	0.01713	0.05316
xy	-0.01182	-0.01535	-0.1547
y^2	0.01378	0.01781	1.222
x^3	0.002539	0.003433	-0.02731
x^2y	-0.005917	-0.007667	0.08967
xy^2	-0.005889	-0.007608	0.09638
y^3	0.00257	0.003501	-0.542
r^2	0.944	0.946	0.991

process. Note, that with enough draws, the average of the stochastic N_{uncut} values converges towards the $1/p_{cut}$ case.

The inversion process is tested on two synthetically generated crystal fabrics: (1) a uniform distribution (Figs. 7) and (2) a unimodal (Type-P) distribution (Fig. 8), with the A-axes aligned preferentially near the horizon and to the north. Both modeled systems utilize a constant crystal shape of A:3, B:1, and C:1, with $n = 3000$ crystals in the cut fabric.

The inverted ODFs are presented in Figs. 7 and 8 (panels a-d in each), and qualitatively illustrate that the inversion methodology is capable of faithfully recreating the uncut fabric. To quantify the inversion fidelity, the J-index and L2 Error between inverted ODFs and the input, uncut fabric (Figs. 7e and 8e-f). As can be observed in the figures, for both the uniform and unimodal fabrics, the cut fabric increases L2 error (ODF_{cut} – ODF_{uncut}). In the case of the uniform fabric, it increases the texture index, though it still falls below $J_{critical}$. The inversion process decreases the associated L2 error.

The spread in imperfect inversion results indicates the associated error with the inversion process. To test the accuracy of the process, these inverted fabric results can be compared directly against the known uncut fabric used as input. Because the uncut fabric is generated via spherical harmonics, it is equivalent to an infinitely large sample size, which affects texture index (Fig. 5). To remove this effect, a similar sample size uncut fabric (ODF_{SSS}) is generated by randomly sampling from the infinite sample size uncut fabric (ODF_{ISS}). Repeating this process ($n = 1000$) allows for

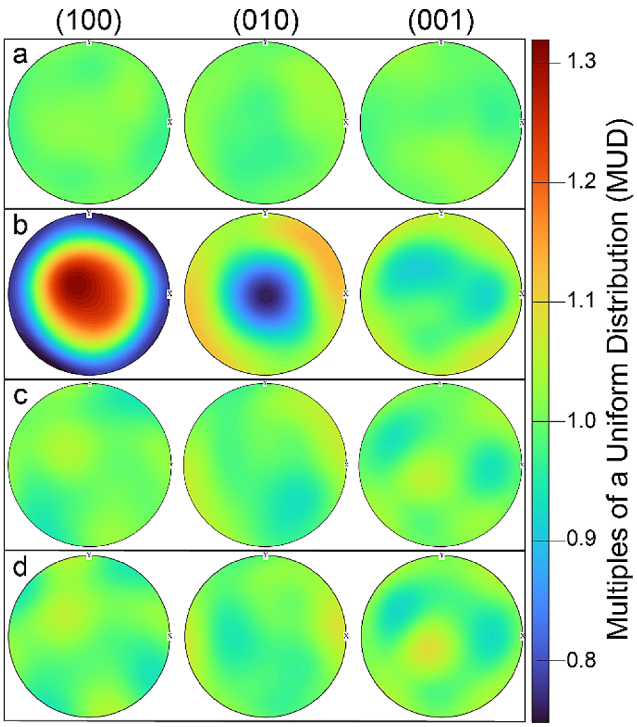

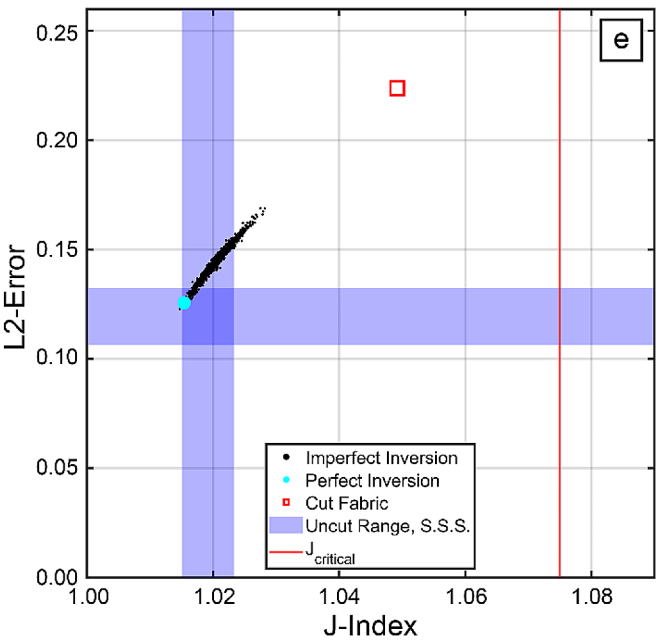

Fig. 7 Inversion results for synthetically generated and cut uniform fabric, for constant crystal shape A: 3, B: 1, C: 1. For ODFs in panels a)-d) colors are coded to MUD, and kept constant for all plots. The inverted ODFs are approximately uniformly distributed (MUD ~ 1 for all orientations). (a) Uncut fabric. (b) Cut fabric. (c) Perfect Inversion. (d) Imperfect Inversion. (e) Fabric quantification, J-index vs. $L2_{error}$ (ODF – ODF_{uncut}) for the inversions of the synthetic uniform ODF model (A:3, B: 1, C:1, $n = 3000$). The uncut fabric ODF is the Uniform ODF, with a J-index of 1. For a similar sample size ($n = 3000$), subsampling from the Uniform ODF generates a 90% confidence interval, with the L2 error measured comparing the similar sample size ODF against the infinite sample size case, uniform ODF (blue region, Uncut Range similar sample size). The inverted ODFs (black dots ($n = 1000$) and blue circle) reduce L2 Error compared to the cut fabric ODF (red square) and overlap the texture strength of a similar sample size uniform fabric

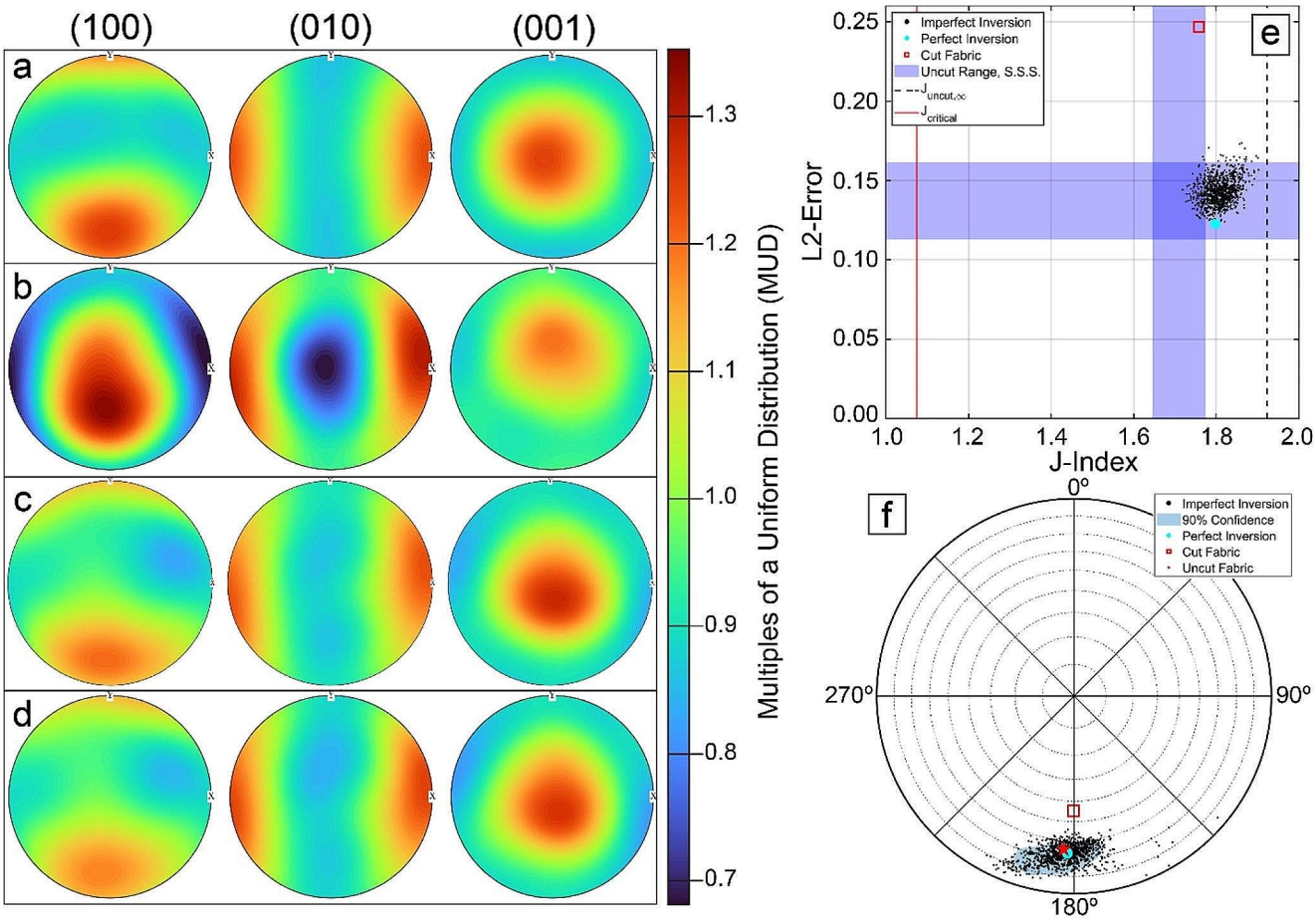

Fig. 8 Inversion results for synthetically generated and cut unimodal fabric, for constant crystal shape A: 3, B: 1, C: 1. For ODFs in panels a-d colors are coded to MUD, and kept constant for all plots. (a) Uncut fabric with A-axis preferentially aligned to the north of the pole figure. (b) Cut fabric, with an apparent fabric that differs from the true, uncut fabric, with A-axes preferentially aligned sub-vertically. (c) Perfect Inversion. (d) Imperfect Inversion. The inverted ODFs return a good approximation of the uncut fabric. (e) J-index vs. $L2_{error}$ (ODF – ODF_{uncut}). The dashed line is the J-Index for the infinite sample size uncut ODF. For a similar sample size ($n = 3000$), subsampling from the Type-P ODF generates a 90% confidence interval, with the L2 error measured comparing the similar sample size ODF against the infinite sample size case, Type-P ODF (blue region, Uncut Range S.S.S.). The inverted ODFs (black dots ($n = 1000$) and blue circle) reduce L2 Error compared to the cut fabric ODF (red square), and imperfect inversions partially overlap the texture strength of the uncut fabric of similar sample size. (f) A-axis mode orientation, plotted in an upper hemisphere stereographic projection. Dashed concentric circles represent 10° zenith contours. The uncut fabric (red star) is approximately oriented to the south (-y direction) with an inclination of 25 degrees. The cut fabric (red square) is inclined at ~45 degrees. The inverted ODFs (black dots and blue circle) reduce the associated orientation error. Confidence intervals (blue and pink shaded regions) generated by the imperfect inversions contain the uncut fabric orientation

the construction of a 90% confidence interval for both the texture-index (J), and L2 error (ODF_{ISS} - ODF_{SSS}). These regions are plotted in blue in Figs. 7e and 8e.

Additionally, for the unimodal, Type-P fabric, the preferred orientation of the inverted fabric can be statistically compared against that of the input fabric (Fig. 8f). The fabric-cut effect induces an apparent (100) preferred orientation inclined roughly 55° from the horizon. The inversion process recovers the uncut fabric orientation reasonably well, with imperfect inversion confidence intervals determined via directional quantile envelope (Kong and Mizera 2012), including the uncut fabric mode.

Application to a natural sample

We apply the preceding tools to an oriented sample from a feeder dike associated with the Columbia River Flood Basalts. In this system, careful interpretation of the observed fabric is essential for determining whether crystallization occurred before flow (i.e., as an entrained load of crystals), or in a static environment, and if a non-uniform fabric exists, accurately determining the directionality of that fabric.

Columbia river flood basalt dike

The Columbia River Flood Basalts are Earth's youngest example of flood basalts (Barry et al. 2013). The main phase of these flows was fed primarily through dikes now residing within the Chief Joseph Dike Swarm, centered on the Wallowa Mountains of Eastern Oregon (Morriss et al. 2020; Petcovic and Grunder 2003; Karlstrom et al. 2019; Reidel and Tolan 2013). Sample PR-1-165 was collected near the margin of a small, ~2 m wide dike, located along the "Rattlesnake Gulch" portion of Highway 129 in Southeastern Washington. The sample was collected using a core drill such that the orientation of the resulting thin section is oriented with the long axis along the strike of the dike, and the plane of the thin section is aligned along the horizon.

Early primary phases within PR-1-165 are roughly equal proportions of plagioclase (< 1 mm) and pyroxene (< 250 μm), generally displaying a subophitic relationship. These phases represent roughly 40% of the sample. The remainder of the sample is very fine-grained (near the optical limit) mesostastic assemblage of plagioclase, pyroxene, iron-titanium oxides, and apatite. Secondary, subsolidus hydrothermal products are observed as amydules and fracture fill. Given the relatively large size of the plagioclase, the narrow width of the dike, and the location of the sample along the margin of the dike, it is reasonable to assume that these crystals were present during the emplacement of the dike and thus were capable of recording flow direction via alignment of long-axes sub-parallel to flow direction.

Thin sections were prepared with a probe-quality polish, followed by an EBSD polish that removes any crystallographic strain imparted from the previous cutting and polishing processes. EBSD analyses were collected using a Hitachi S-3400 SEM with an Oxford EBSD system at the Ray and Mary Wilcox SEM Lab of the University of Wisconsin-Madison. The analyses were montaged, large area maps, with an accelerating voltage of 30 keV and specimen tilt of 70 degrees. The step size was 15 μm, with a resulting pixel area of 225 μm^2. The EBSD dataset was processed using the MTEX toolkit (Bachmann et al. 2010). While data representing a suite of phases was collected, we focused solely on plagioclase (indexed utilizing the pattern of 'Oligoclase-An28'). Plagioclase grain boundaries were drawn using the default misorientation threshold of 10°. Polysynthetic twins are identified and merged using misorientations greater than 178°. The average orientation of the merged grain is calculated, and grains smaller than 5 pixels are removed. The orientations of these processed grains are used to generate the cut ODF and resulting J-index (J = 1.344). As an aside, the utility of this automated approach is highlighted by the robustness of these datasets, with the dataset comprised of several thousand crystals ($n = 2927$). The grain boundaries, represented by a polygon, are measured using principal components.

These measurements are input into ShapeCalc to estimate crystal morphology (L: 3.8, I: 2.2, with A = L, C = I). This crystal shape estimate allows for comparison of fabric strength against $J_{critical}$, utilizing Eq. 6 and coefficients from Table 1. With this shape as input, $J_{critical} = 1.063$ (using A = L, C = I, and column 2 of Table 1), and $J_{critical} = 1.0583$ (using values of L and I, column 3 of Table 1). The measured ODF J-Index of the fabric exceeds $J_{critical}$ for the estimated crystal shape, indicating that the uncut fabric is non-uniform.

The ODF derived from EBSD analysis of PR-1-165 results in a smeared pole/partial girdle associated with the A-axis (Fig. 9a). Using A = L and C = I for an elongate, tabular crystal shape, the inversion process results in a horizontally inclined partial girdle along the A-axis, (100), and a vertical pole along the B-axis, (010) (Fig. 9b-c).

The mode for A-axis, (100) orientations of the inverted ODF (Fig. 9d) reveal a dense grouping imperfect inversion results clustered around the perfect inversion result. This dense grouping falls near the horizon, aligned subparallel to the dike strike. This is notable, considering the raw EBSD-derived ODF results in a nearly vertical mode. This difference between measured fabric and inverted fabric could result in vastly different interpretations of the system, specifically: was magma flow vertical (uncorrected EBSD data), or lateral (inverted EBSD data)?

However, comparing the resulting large spread of the confidence interval in PR-1-165 (Fig. 9d) against the relatively tight confidence interval of controlled synthetic samples (Fig. 8f), suggests fundamental differences between these two systems. While addressing this further is beyond the scope of this contribution, the inversion methodology utilized here is built on the assumption that the population of crystals is fit by a singular crystal shape. In the synthetically derived samples, constant crystal shape is controlled for, while in natural samples may significantly depart from this condition.

Overall, the results show that the fabric cut effect can be significant for EBSD datasets of magmatic systems. In igneous systems, fabric tends to be relatively weak–significantly weaker than in metamorphic systems (Satsukawa et al. 2013). Indeed, much of the EBSD investigations of igneous systems have focused on characterizing and interpreting systems where magmatic fabric is well-developed, such as layered mafic intrusions and cumulate-rich systems (Holness et al. 2012, 2017; Cheadle and Gee 2017; Vukmanovic et al. 2018, 2019; Bertolett et al. 2019), and fluxion gabbros deep within ophiolite sections (Jousselin et al. 2012; Henry et al. 2021). However, these are exceptional cases, and igneous systems that have crystallized primarily under static

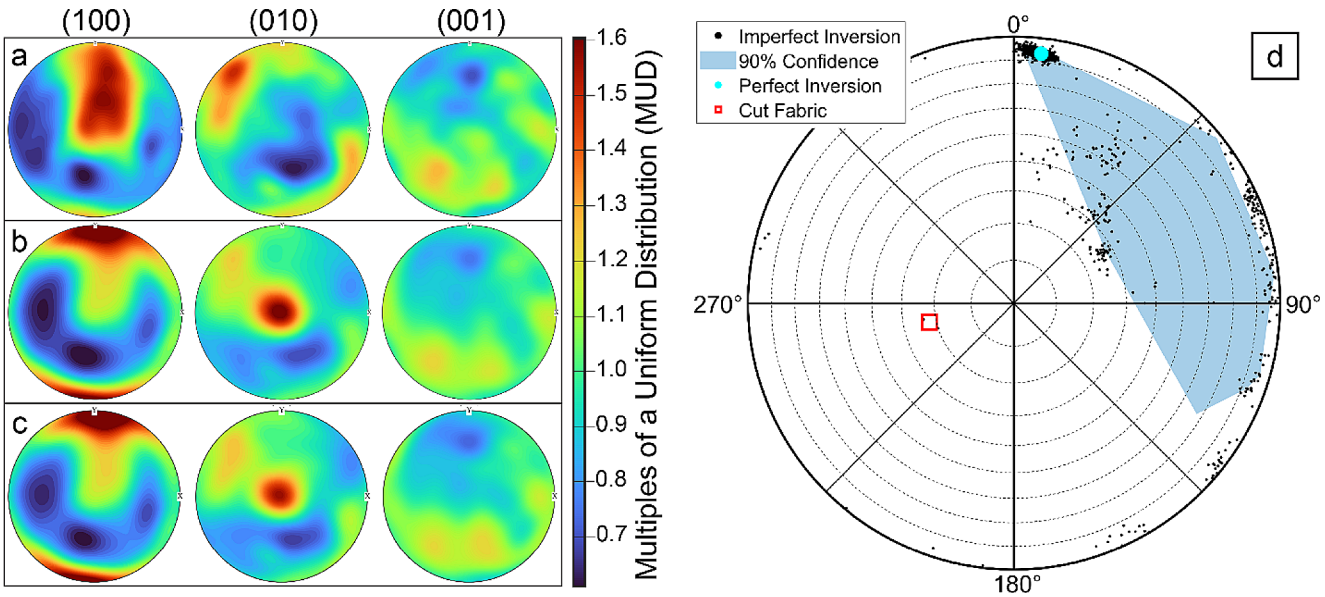

Fig. 9 Inversion results for PR-1-165. Colors are coded to MUD, and kept constant for all plots. ShapeCalc crystal shape estimate is A: 3.8, B: 1, C: 2.2. (a) EBSD derived fabric. Fabric with A-axis preferentially aligned to the north of the pole figure, and sub-vertically arranged. (b) Perfect Inversion. (c) Imperfect Inversion. (d) A-axis mode orientation for PR-1-165, plotted in an upper hemisphere stereographic projection. Dashed concentric circles represent 10° zenith contours. Values for the inverted fabrics (black dots and blue circle) depart significantly from that of the cut fabric, represented here by EBSD data (red square). The bulk of the imperfect inversion A-axis mode orientations and the perfect inversion (blue circle) are roughly in the horizontal plane, aligned nearly parallel to dike strike. However, the confidence interval is large, and thus, the true fabric of the rock is poorly constrained

conditions may have little to no crystal alignment. Alternatively, shearing under granular conditions may result in complex fabrics strongly developed along bands but weakly developed in bulk (Fu and Dafalias 2010). In these systems in particular, carefully correcting for fabric-cut effect can impact the scientific interpretation in terms of the fabric strength and the 3D crystal orientation patterns.

Discussion

Our results and analysis with synthetic samples directly address the primary motivating question for this study. *There are clear stereological biases that can be present when analyzing the crystal orientation datasets from EBSD, i.e. the fabric-cut effect*. We also develop and demonstrate a method to invert for this (assuming the fabric-cut effect can be decoupled with the shape- and size-cut effect) using the EBSD data. We anticipate that this fabric-cut effect is a significant source of bias in systems with weak fabric (e.g., magmatic fabric), or seemingly strong fabrics at low sample size (Fig. 5), but is present to some extent in all EBSD orientational data. If meaningful interpretations of dynamic processes are to be made from EBSD-derived orientations, then the fabric-cut effect needs to be corrected quantitatively to remove this bias.

Towards a comprehensive, open source textural toolkit

However, as we apply the inversion method to natural samples, we need to be strongly cognizant of the inherent assumptions in the traditional textural analyses that correct for the different cut effects independently. For example, a typical workflow is to first invert for crystal shape (i.e., shape-cut effect, CSDslice: Morgan and Jerram 2006; ShapeCalc: Mangler et al. 2022), then using this as input, invert for crystal size distribution (i.e., size- and size-distribution-cut effects, CSDCorrections: Higgins 2000). As a first approach towards investigating the fabric cut effect, we have followed an approach motivated by similar existing methodologies in this study. We solve for the fabric cut effect independently of the other cut effects and thus assume that the different cut effects are sequentially separable. Therefore, mathematically the assumption is that the full cut effect correction (f) can be represented as a series of sequential functions:

$$f\left(shape, orient.\right) = f_x\left(shape\right) \times f_y\left(shape_0, orient.\right) \times f_z \quad (6)$$

Where f_x is the shape cut effect, f_y is the fabric cut effect with shape fixed, and f_z is the size and size distribution cut effect with shape and orientation fixed. In natural datasets, other effects may also need to be considered. For example,

the spatial interdependence of multiple particle populations leads to correlations and constraints on particle orientation so as to not physically overlap. However, for simplicity, the analysis tools assume that the data represents a single coherent population (as chosen by the user) and these spatial variations can be ignored in the inversion process.

We consider a shape-disperse synthetic example as an example of how these assumptions affect the results in samples with multiple overlapping crystal populations. Three different crystal morphologies are chosen such that the long axis of the crystal is tied to a separate crystallographic axis for each subpopulation (A1: 3, B1: 1, C1: 1; A2: 1, B2: 3, C2: 1; A3: 1, B3: 1, C3: 3) yet the overall crystal aspect ratio remains constant (i.e., L: 3, I: 1, S: 1). The cut-plane samples each population of crystals in equal proportions (n1 = n2 = n3 = 1000). The orientations of each population of crystals are sampled from the uniform ODF (Fig. 10a).

These chosen crystal shapes, system, and fabric parallel the constant crystal shape model illustrated in Fig. 3b-d. After imposing the fabric-cut effect for this mixed population of crystals, a weak structure appears (Fig. 10b) with three approximately equivalent inclined girdles along each crystallographic axis, with each girdle circumscribing the vertical. This pattern is strikingly different from the pattern that emerges when the crystal shape is constant (Fig. 3b-d).

In addition to sampling orientations of the cut crystals, the widths and lengths of the 2D crystal intersection polygon were measured (bounding box method). From these measurements, a reasonably accurate estimate of crystal shape is provided by ShapeCalc: a long axis of 3.2 and an intermediate axis of 1, and a coefficient of determination of 0.997. This result is not unexpected. Current crystal shape algorithms do not utilize 3D crystallographic data, and disregarding crystallographic axes, the crystal subpopulations are identical in morphology (i.e., L:3, I: 1, S: 1). However,

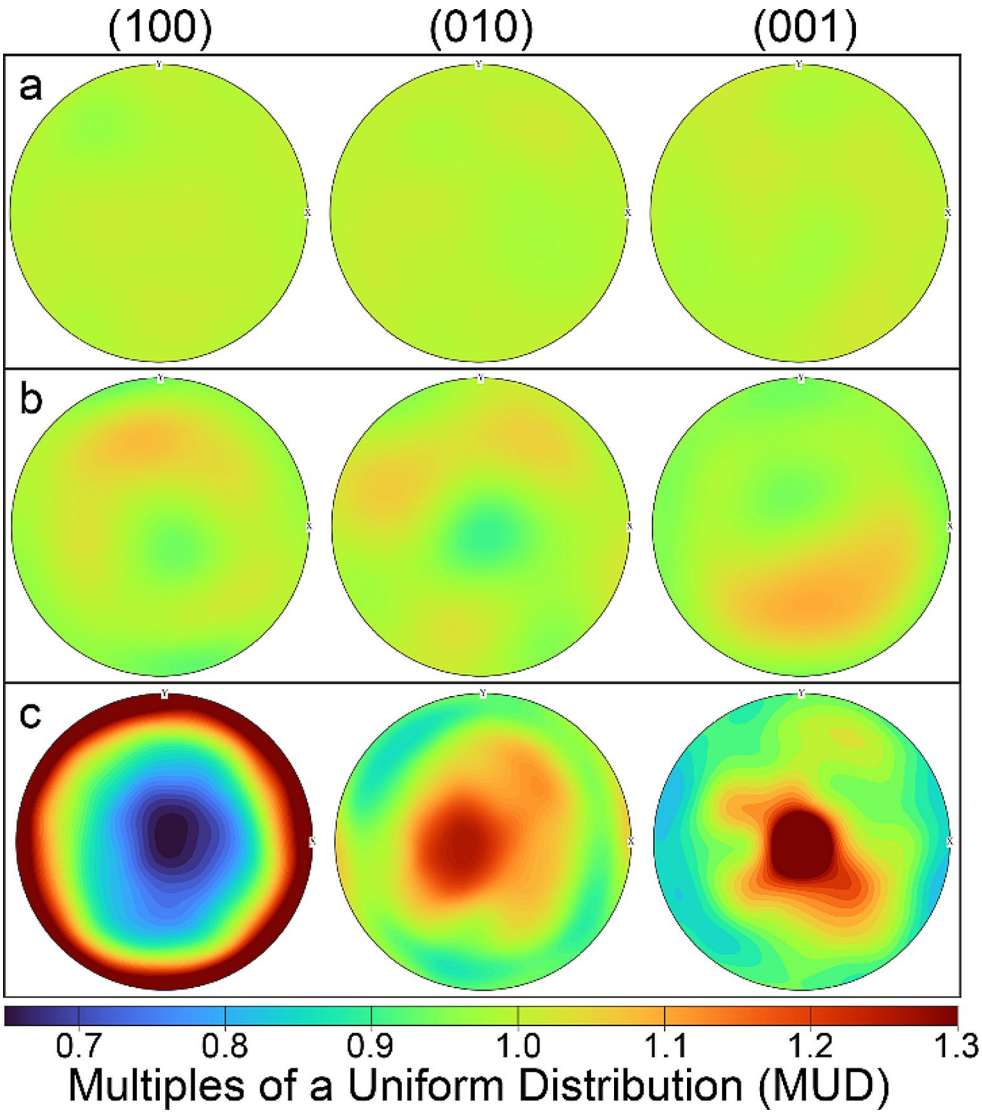

Fig. 10 Synthetic model results for three merged subpopulations defined by different crystal shapes. Each population is equal in the number of sampled, cut crystals ($n = 1000$), the same orientation sampling space (i.e., the uniform ODF), and with crystal shapes equivalent to those in Fig. 3b-d, (L: 3, I: 1, S:1). The colorbar is kept constant for both ODFs, and is equivalent to the scale used in Fig. 3. (a) The true fabric of the system (uncut fabric) displays no discernible structure across each crystallographic axis, with MUD ~ 1. (b) The ODF after imposing the fabric-cut effect. (c) Perfect inversion results, using A: 3, B: 1, C: 1

tying this crystal shape estimate to any permutation of crystallographic axes invariably results in an incorrect inversion, where a horizontal girdle for the chosen crystallographic long axis, and two vertical poles for the intermediate and short axes. This effect is illustrated in Fig. 10c, following our earlier convention of A = L, C = I.

While this modeled system is arguably unrealistic in specifics, these results clearly illustrate that the *a priori* assumption of a single population and independent separation of full cut effect correction (f, Eq. 6) into a series of sequential functions may only sometimes be valid for natural settings. A potential signature of this issue could be that in the Columbia River dike sample above, we find results that differ from what would be expected from the controlled conditions of synthetic fabric inversions i.e., a reasonably large confidence interval (Fig. 8f). Furthermore, in the inverted ODFs presented in Fig. 9b-c, a vertical pole is present along the B-axis. This result, if correct, is surprising since it doesn't match with the expectation of particle orientation dynamics in viscous flowing fluids within an open fracture (e.g., Vachon et al. 2021). Alternatively, our inversion process, which assumes a constant crystal shape, may not be correct due to an unconstrained dispersive crystal shape and fabric across size populations in the sample.

Overall, the results shown in the paper and the synthetic results show that the fabric-cut effect may not be fully decoupled in a multiplicative manner (i.e., Eq. 6). This indicates some critical challenges with full inversion of underlying 3D rock texture using existing stereological methods and revisiting the methods. Although the geoscience community, especially petrology, has been very good at developing codes for stereological analysis of thin sections, some key issues remain, while new issues are on the horizon.

- Currently, each stereographic inversion is performed in a piecemeal fashion, through a variety of freely available texture inversion algorithms. There is presently a need for fully integrated software capable of holistically analyzing textural information.
- A clear description of assumptions utilized in texture inversion algorithms is generally unavailable, leaving ambiguity about whether results accurately represent sample textures, thus decreasing confidence in results.
- Source code for texture inversion algorithms is generally not available. Thus, it is challenging to assess which particular shape descriptors are best suited for stereological correction (e.g., best-fit ellipse, Feret diameter, bounding rectangle, crystal area, perimeter, circularity or some subset of them together).
- The lack of available source code also poses challenges to extending the modeling frameworks to include more information such as spatial distribution of the crystals and orientations (in 2D as well as orientation data from EBSD) when performing stereological corrections/inversions. Consequently, significant barriers to entry exist for non-experts to use these methods correctly and modify the codes for different applications. This is critical for applications where the underlying assumptions may only partially be valid and sensitivity analysis is necessary to show the robustness of the results.

These considerations motivate future work toward an integrated textural toolbox that is: (1) capable of addressing a variety of textural analyses, (2) modular and extensible to suit specific use cases, and (3) publicly available, with open-source code that is well-documented and thoroughly benchmarked.

Conclusion

The EBSD method offers advantages over traditional thin-section-based analyses. Grain measurements are automated and reproducible, and an additional data stream of grain orientation is provided. However, a cut effect skews these results due to the nature of acquiring this orientation data from a thin section. We have investigated this effect and found that it can significantly skew the measured fabric from the true fabric. The fabric-cut effect must be accounted for to accurately represent any quantification of fabric collected using EBSD data.

The proper correction for realistic systems is tied to the shape-size-orientation, three-dimensional probability distributions. We have shown the effects in simplified models, but there is no inherent reason for these simplifying assumptions to be true. We conclude by suggesting that a more robust correction for these cut effects, will require simultaneous correction.

Acknowledgements We thank Michael Higgins and an anonymous reviewer for their helpful comments. Support was provided by the National Science Foundation, award number: 2112035.

Author contributions All authors contributed to the study's conception, design, and data collection. Currier wrote the first draft, and all authors commented during the evolution of the manuscript. All authors have read and approved the final manuscript.

Funding Support was provided by the National Science Foundation, award number: 2112035.

Declarations

Financial interests The authors have no financial or proprietary interests in any material discussed in this article.

References

Andreani M, Luquot L, Gouze P, Godard M, Hoise E, Gibert B (2009) Experimental study of carbon sequestration reactions controlled by the percolation of CO2-rich brine through peridotites. Env Sci Tech 43:1226–1231. https://doi.org/10.1021/es8018429

Bachmann F, Hielscher R, Schaeben H (2010) Texture analysis with MTEX—Free and open source software toolbox. Solid State Phenom 160:63–68. https://doi.org/10.4028/www.scientific.net/SSP.160.63

Bain AA, Calder ES, Cortes JA, Cortes GP, Loughlin SC (2019) Textural and geochemical constraints on andesitic plug emplacement prior to the 2004–2010 vulcanian explosions at Galeras volcano, Colombia. Bull Volc 81:1–25. https://doi.org/10.1007/s00445-018-1260-y

Barry TL, Kelley SP, Reidel SP, Camp VE, Self S, Jarboe NA, Duncan RA, Renne PR, Ross ME, Wolff JA, Martin BS (2013) Eruption chronology of the Columbia River Basalt Group. Spec Pap Geol Soc Am Special Paper 497:45–66

Bernard RE, Chin EJ, Murphy C (2023) Melt-assisted deformation in the lower crust of an active plate boundary, Baja California. Lithos 438–439:106975. https://doi.org/10.1016/j.lithos.2022.106975

Bertolett EM, Prior DJ, Gravley DM, Hampton SJ, Kennedy BM (2019) Compacted cumulates revealed by electron backscatter diffraction analysis of plutonic lithics. Geology 47:445–448. https://doi.org/10.1130/G45616.1

Britton TB, Jiang J, Guo Y, Vilalta-Clemente A, Wallis D, Hansen LN, Winkelmann A, Wilkinson AJ (2016) Tutorial: Crystal orientations and EBSD—Or which way is up? Mat Char 117:113–126. https://doi.org/10.1016/j.matchar.2016.04.008

Brugger CR, Hammer JE (2010) Crystal size distribution analysis of plagioclase in experimentally decompressed hydrous rhyodacite magma. Earth Planet Sci Lett 300:246–254. https://doi.org/10.1016/j.epsl.2010.09.046

Casale G, Levine JSF, Economou J (2023) Extracting quartz deformation fabrics from polymineralic rocks. J Struct Geol 173:104893. https://doi.org/10.1016/j.jsg.2023.104893

Cheadle MJ, Gee JS (2017) Quantitative textural insights into the formation of gabbro in mafic intrusions. Elements 13:409–414. https://doi.org/10.2138/gselements.13.6.409

Cone KA, Wendlandt RF, Pfaff K, Orlandini OF (2020) Texture constraints on crystal size distribution methodology: an application to the Laki fissure eruption. Am Min 105:585–598. https://doi.org/10.2138/am-2020-7007

Cross AJ, Prior DJ, Stipp M, Kidder S (2017) The recrystallized grain size piezometer for quartz: an EBSD-based calibration. Geophys Res Lett 44:6667–6674. https://doi.org/10.1002/2017GL073836

Currier RM, Ashauer ZM, Norfleet MA (2019) Textural analyses of classical rapakivi granites: texture formation through coarsening, size-selective replacement, and stirring. Precam Res 321:1–12. https://doi.org/10.1016/j.precamres.2018.11.020

Dunbar NW, Jacobs GK, Naney MT (1995) Crystallization processes in an artificial magma: variations in crystal shape, growth rate and composition with melt cooling history. Contrib Min Petrol 120:412–425. https://doi.org/10.1007/BF00306518

Fossen H, Cavalcante GCG (2017) Shear zones—A review. Earth Sci Rev 171:434–455. https://doi.org/10.1016/j.earscirev.2017.05.002

Frothingham MG, Mahan KH, Schulte-Pelkum V, Goncalves P, Zucali M (2023) Confronting solid-state shear bias; magmatic fabric contribution to crustal seismic anisotropy. Geophys Res Lett 50:102399. https://doi.org/10.1029/2022GL102399

Fu P, Dafalias YF (2010) Fabric evolution within shear bands of granular materials and its relation to critical state theory. Int J Num Anal Meth Geomech 35:1918–1948. https://doi.org/10.1002/nag.988

Gibert B, Seipold U, Tommasi A, Mainprice D (2003) Thermal diffusivity of upper mantle rocks: influence of temperature, pressure, and the deformation fabric. J Geophys Res 108. https://doi.org/10.1029/2002JB002108

Hemkemeyer M, Dohrmann AB, Christensen BT, Tebbe CC (2018) Bacterial preferences for specific soil particle size fractions revealed by community analyses. Front Microbio 9. https://doi.org/10.3389/fmicb.2018.00149

Henry H, Kaczmarek MA, Ceuleneer G, Tilhac R, Griffin WL, O'Reilly SY, Gregoire M, Le Sueur E (2021) The microstructure of layered ultramafic cumulates: Case study of the Bear Creek intrusion, Trinity ophiolite, California, USA. Lithos 388–389. https://doi.org/10.1016/j.lithos.2021.106047

Higgins MD (1994) Numerical modeling of crystal shapes in thin sections: estimation of crystal habit and true size. Am Min 79:113–119

Higgins MD (2000) Measurement of crystal size distributions. Am Min 85:1105–1116. https://doi.org/10.2138/am-2000-8-901

Higgins MD (2002) A crystal size-distribution study of the Kiglapait layered mafic intrusion, Labrador, Canada: evidence for textural coarsening. Contrib Min Petrol 144:314–330. https://doi.org/10.1007/s00410-002-0399-9

Holness MB, Sides R, Prior DJ, Cheadle M, Upton BGJ (2012) The peridotite plugs of rum: Crystal settling and fabric development in magma conduits. Lithos 134–135:23–40. https://doi.org/10.1016/j.lithos.2011.11.024

Holness MB, Vukmanovic Z, Mariani E (2017) Assessing the role of compaction in the formation of adcumulates: a microstructural perspective. J Petrol 58:643–674. https://doi.org/10.1093/petrology/egx037

Holness MB, Vukmanovic Z, O'Driscoll B (2023) The formation of chromite chains and clusters in igneous rocks. J Petrol 64:1–24. https://doi.org/10.1093/petrology/egac124

Howard V, Reed MG (1998) Unbiased stereology: three-dimensional measurement in microscopy. Bios Scientific, Oxford. https://doi.org/10.4324/9780203006399

Jenkins MC, Mungall JE, Zientek ML, Butak K, Corson S, Holick P, McKinley R, Lowers H (2022) The geochemical and textural transition between the reef Package and its hanging wall, Stillwater Complex, Montana, USA. J Petrol 63:1–30. https://doi.org/10.1093/petrology/egac053

Jerram DA, Higgins MD (2007) 3D analysis of rock textures: quantifying igneous microstructures. Elements 3:239–245. https://doi.org/10.2113/gselements.3.4.239

Jerram DA, Davis GR, Mock A, Charrier A, Marsh BD (2010) Quantifying 3D populations, packing and layering in shallow intrusions: a case study from the Basement Sill, Dry valleys, Antarctica. Geosphere 6:537–548. https://doi.org/10.1130/GES00538.1

Jousselin D, Morales LFG, Nicolle M, Stephant A (2012) Gabbro layering induced by simple shear in the Oman Ophiolite Moho transition zone. Earth Planet Sci Lett 331:55–66. https://doi.org/10.1016/j.epsl.2012.02.022

Karlstrom L, Murray KE, Reiners PW (2019) Bayesian Markov-Chain Monte Caro inversion of low-temperature thermochronology around two 8–10 m wide Columbia River Flood basalt dikes. Front Earth Sci 7. https://doi.org/10.3389/feart.2019.00090

Kong L, Mizera I (2012) Quantile tomography: using quantiles with multivariate data. Stat Sinica 22:1589–1610. https://www.jstor.org/stable/24310188

Koyama Y, Wallis SR, Nagaya T (2023) Subduction plate interface shear stress associated with rapid subduction at deep slow earthquake depths: example from the Sanbagawa belt, Southwest Japan. EGUsphere Sol Earth 15:143–166. https://doi.org/10.5194/se-15-143-2024

Lanzafame G, Iezzi G, Mancini L, Lezzi F, Mollo S, Ferlito C (2017) Solidification and turbulence (non-laminar) during magma ascent:

insights from 2D and 3D analyses of bubbles and minerals in an Etnean Dyke. J Petrol 58:1511–1533. https://doi.org/10.1093/petrology/egx063

Magee C, O'Driscoll B, Chambers AD (2010) Crystallization and textural evolution of a closed-system magma chamber: insights from a crystal size distribution study of the Lilloise layered intrusion, East Greenland. Geol Mag 147:363–379. https://doi.org/10.1017/S0016756809990689

Mainprice D, Bachmann F, Hielscher R, Schaeben H (2015) Descriptive tools for the analysis of texture projects with large datasets using MTEX: strength, symmetry and components. Geol Soc Lond Spec Pub 409:251–271. https://doi.org/10.1144/SP409.8

Mangler MF, Humphreys MCS, Wadsworth FB, Iveson AA, Higgins MD (2022) Variation of plagioclase shape with size in intermediate magmas: a window into incipient plagioclase crystallisation. Contrib Min Petrol 177. https://doi.org/10.1007/s00410-022-01922-9

Marsh BD (1998) On the interpretation of crystal size distributions in magmatic systems. J Petrol 39:553–599. https://doi.org/10.1093/petroj/39.4.553

Mock A, Jerram DA (2005) Crystal size distributions (CSD) in three dimensions: insights from the 3D reconstruction of a highly porphyritic rhyolite. J Petrol 46:1525–1541. https://doi.org/10.1093/petrology/egi024

Morgan DJ, Jerram DA (2006) On estimating crystal shape for crystal size distribution analysis. J Volcanol Geotherm Res 154:1–7. https://doi.org/10.1016/j.jvolgeores.2005.09.016

Morriss MC, Karlstrom L, Nasholds MWM, Wolff JA (2020) The Chief Joseph dike swarm of the Columbia River flood basalts, and the legacy data set of William H. Taubeneck Geosph 16:1082–1106. https://doi.org/10.1130/GES02173.1

Muncill GE, Lasaga AC (1988) Crystal-growth kinetics of plagioclase in igneous systems: isothermal H2O-saturated experiments and extension of a growth model to complex silicate melts. Am Min 73:982–992

Ngonge ED, Archanjo CJ, Hollanda MHBM (2013) Plagioclase crystal size distribution in some tholeiitic mafic dykes in Cabo Frio-Buzios, Rio De Janeiro, Brazil. J Volcanol Geotherm Res 255:26–42. https://doi.org/10.1016/j.jvolgeores.2013.01.009

Petcovic HL, Grunder AL (2003) Textural and thermal history of partial melting in tonalitic wallrock at the margin of a basalt dike, Wallowa Mountains, Oregon. J Petrol 44:2287–2312. https://doi.org/10.1093/petrology/egg078

Phillips JC, Humphreys MCS, Daniels KA, Brown RJ, Witham R (2013) The formation of columnar joints produced by cooling in basalt at Staffa, Scotland. Bull Volcanol 75. https://doi.org/10.1007/s00445-013-0715-4

Polacci M, Arzilli F, La Spina G, Le Gall N, Cai B, Hartley ME, Di Genova D, Vo NT, Nonni S, Atwood C, Llewelling EW, Lee PD, Burton MR (2018) Crystallisation in basaltic magmas revealed via in situ 4D synchrotron X-ray microtomography. Sci Rep 8. https://doi.org/10.1038/s41598-018-26644-6

Prikryl R (2006) Assessment of rock geomechanical quality by quantitative rock fabric coefficients: limitations and possible source of misinterpretations. Eng Geol 87:149–162. https://doi.org/10.1016/j.enggeo.2006.05.011

Rehman HU, Mainprice D, Barou F, Yamamoto H, Wei C, Zafar T, Khan T (2023) Crystallographic preferred orientations and microtexture of the himalayan eclogites revealing records of syn-deformation peak metamorphic stage and subsequent exhumation. J Struct Geol 167:104792. https://doi.org/10.1016/j.jsg.2023.104792

Reidel SP, Tolan TL (2013) The Grande Ronde Basalt, Columbia River Basalt Group. Spec Pap Geol Soc Am 497:117–153

Salisbury MJ, Bohrson WA, Clynne MA, Ramos FC, Hoskin P (2008) Multiple plagioclase crystal populations identified by crystal size distribution and in situ chemical data: implications for timescales of magma chamber processes associated with the 1915 eruption of Lassen Peak, CA. J Petrol 49:1755–1780. https://doi.org/10.1093/petrology/egn045

Saltikov SA (1967) The determination of the size distribution of particles in an opaque material from the measurement of the size distribution of their sections. In: Elias H (ed) Stereology. Springer-, New York, pp 163–173

Satsukawa T, Ildefonse B, Mainprice D, Morales LFG, Michibayashi K, Barou F (2013) A database of plagioclase crystal preferred orientations (CPO) and microstructures-implications for CPO origin, strength, symmetry and seismic anisotropy in gabbroic rocks. Solid Earth 4:511–542. https://doi.org/10.5194/se-4-511-2013

Underwood EE (1969) Stereology, or the quantitative evaluation of microstructures. J Micro 89:161–180. https://doi.org/10.1111/j.1365-2818.1969.tb00663.x

Urumovic K, Urumovic K (2014) The effective porosity and grain size relations in permeability functions. Hydrol Earth Sys Sci Disc 11:6675–6714. https://doi.org/10.5194/hessd-11-6675-2014

Vachon R, Bazargan M, Hieronymus CF, Ronchin E, Almqvist B (2021) Crystal rotations and alignment in spatially varying magma flows: 2-D examples of common subvolcanic flow geometries. Geophys J Int 226:709–727. https://doi.org/10.1093/gji/ggab127

Vinet N, Higgins MD (2011) What can crystal size distribution and olivine compositions tell us about magma solidification processes inside Kilauea Iki lava lake. Hawaii? J Volcanol Geotherm Res 208:136–162. https://doi.org/10.1016/j.jvolgeores.2011.09.006

Vukmanovic Z, Holness MB, Monks K, Anderson JCO (2018) The Skaergaard trough layering: sedimentation in a convecting magma chamber. Contrib Min Petrol. https://doi.org/10.1007/s00410-018-1466-1

Vukmanovic Z, Holness MB, Stock MJ, Roberts RJ (2019) The creation and evolution of crystal mush in the Upper Zone of the Rustenburg Layered Suite, Bushveld Complex, South Africa. J Petrol 60:1523–1542. https://doi.org/10.1093/petrology/egz038

Wieser PE, Vukmanovic Z, Kilian R, Ringe E, Holness MB, Maclennan J, Edmonds M (2019) To sink, swim, twin, or nucleate: a critical appraisal of crystal aggregation processes. Geology 47:948–952. https://doi.org/10.1130/G46660.1